Bull. Mater. Sci. (2021)44:289
https://doi.org/10.1007/s12034-021-02574-4

Study of self-powered and broadband photosensing properties of CdS/PbS-decorated TiO_2 nanorods/reduced graphene oxide junction

NITUMONI DEKA, PINAK CHAKRABORTY, DULAL CHANDRA PATRA, SAURAB DHAR and SUVRA PRAKASH MONDAL*
Department of Physics, National Institute of Technology, Agartala 799046, India
*Author for correspondence (suvraphy@gmail.com; suvra.phy@nita.ac.in)

MS received 28 May 2021; accepted 23 August 2021

Abstract. Self-powered broadband photodetector was fabricated using PbS/CdS-decorated TiO_2 nanorods (NRs). TiO_2 NRs were grown using hydrothermal method and CdS/PbS layers were deposited by chemical bath deposition process. Metal-free top electrode of the photodetector was prepared using chemically reduced graphene oxide (rGO). PbS/CdS-decorated TiO_2 NRs based photodetector showed significant photocurrent over broad spectral range. The maximum responsivity (R_λ) and detectivity (D_λ) of the photodetector at zero bias was obtained, $\sim$0.34 A W^{-1} and $\sim$162742.42 $Hz^{1/2}$ W^{-1}, respectively, at 400 nm. TiO_2/CdS/PbS/rGO device showed sharp rise and decline of photocurrent under ON/OFF of white light. This device also demonstrated excellent self-powered nature with open circuit voltage $\sim$0.40 V, short circuit current $\sim$0.077 mA and power conversion efficiency $\sim$0.16%.

Keywords. TiO_2 nanorods; CdS nanoparticles; PbS nanoparticles; reduced graphene oxide (rGO); self-powered photodetector; responsivity (R_λ) and detectivity (D_λ).

1. Introduction

One-dimensional (1D) TiO_2 nanostructured materials such as nanorods (NRs), nanowires and nanotubes have received a great deal of attention during the last decade because of their unique physical, chemical and optical properties, and utilization in a variety of applications, such as photocatalysis, dye-sensitized solar cells, and sensors [1–4]. TiO_2 is a large bandgap semiconductor with bandgap $\sim$3.2 eV and particularly important in optoelectronic devices such as UV detectors and solar cells [5–8]. Since TiO_2 have limited photo-absorption in visible range, it is difficult to fabricate broadband photodetectors using pristine NRs. To achieve photoabsorption in wide spectral range, wide bandgap metal oxides are often sensitized with low bandgap chalcogenide semiconductors, such as PbS, PbSe, CdS, CdSe, etc. [9–15]. Most of these semiconductors exhibit excellent size tuneable optical absorption in wide spectral region. Nowadays, several research works have been focused on the fabrication of self-powered photodetectors, which can be operated without the applied external bias [16–19]. Self-powered broadband photodetectors are particularly attractive for applications in next-generation nanodevices, which can be operated wirelessly and independently [20–22]. Gao *et al* [5] reported self-powered UV photodetector using NiO/TiO_2 heterojunction grown on fluorine-doped tin oxide (FTO) substrate. They obtained responsivity $\sim$1.34 and $\sim$5.66 mA W^{-1} in case of NiO/TiO_2 NR and NiO/TiO_2 NRs/TiOx samples respectively, with rise time less than 0.1 s. Xie and co-workers [23] studied photoelectrochemical-based self-powered photodetector using SnO_2/TiO_2 NR arrays. The photodetector parameters such as responsivity, rise time and decay time were found to be $\sim$145 A W^{-1}, $\sim$0.037 and 0.015 s, respectively. Although, TiO_2-based UV photodetectors were studied by various researchers, however, there is no report available on self-powered broadband photodetector using 1D TiO_2 nanostructures.

In this research, we have studied self-powered broadband photodetector using CdS/PbS nanoparticle-decorated TiO_2 NRs. TiO_2 NRs were synthesized on FTO-coated glass substrates. Top electrical contacts of the devices were made using chemically grown reduced graphene oxide (rGO) layers instead of conventional metal electrodes. Self-powered photosensing nature of TiO_2 NRs/CdS/PbS device has been demonstrated in our present study. The photodetector parameters of the fabricated device have been investigated in detail.

Supplementary Information: The online version contains supplementary material at https://doi.org/10.1007/s12034-021-02574-4.

Published online: 27 November 2021

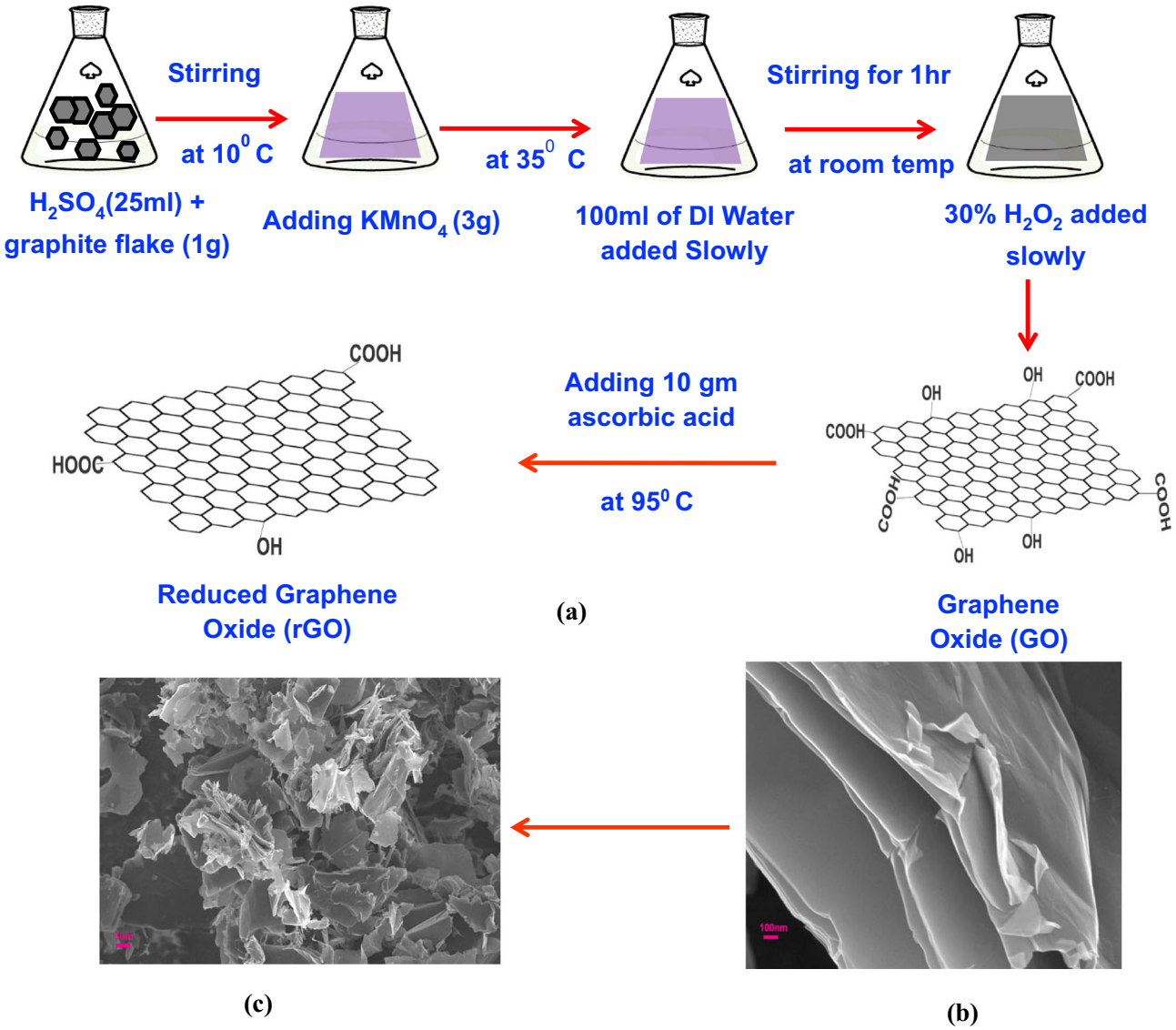

Figure 1. (**a**) Schematic representation for the preparation of graphene oxide (GO) and reduced graphene oxide (rGO). SEM micrographs of (**b**) GO and (**c**) rGO powders.

2. Experimental

TiO_2 NRs were synthesized on FTO-coated glass substrates using hydrothermal technique [7]. As-grown NRs were annealed at 500°C for 1 h to improve the crystallinity. Nanocrystalline CdS layers were deposited on TiO_2 NRs using chemical bath deposition process (CBD). In this method, 0.025 M of cadmium acetate, 0.1 M of ethylenediamine and 0.1 M thiourea were mixed in 100 ml deionized (DI) water and the solution was heated at 60°C. During CdS attachment, TiO_2 NRs were dipped in the prepared solution for 10 min at 60°C. Afterwards, lead sulphide layers was deposited on CdS-decorated TiO_2 NRs using similar CBD process. At first, an aqueous solution was prepared by dissolving 0.05 M lead nitrate $(PbNO_3)_2$, 0.04 M triethanolamine and 0.02 M NaOH in a beaker of 100 ml DI water. On the other hand, 0.06 M thiourea $[CS(NH_2)_2]$ was dissolved in 100 ml DI water in another beaker. The above two solutions were mixed thoroughly and the solution temperature was maintained at 40°C. Subsequently, CdS-decorated TiO_2 NRs were dipped slowly in the solution for 1 h to deposit PbS layer. The control sample TiO_2 NRs/PbS was also prepared using similar CBD process as described above. The TiO_2 NRs on FTO substrates were dipped in the precursor solution for 1 h at 40°C during CBD growth. The pH of the solution was maintained

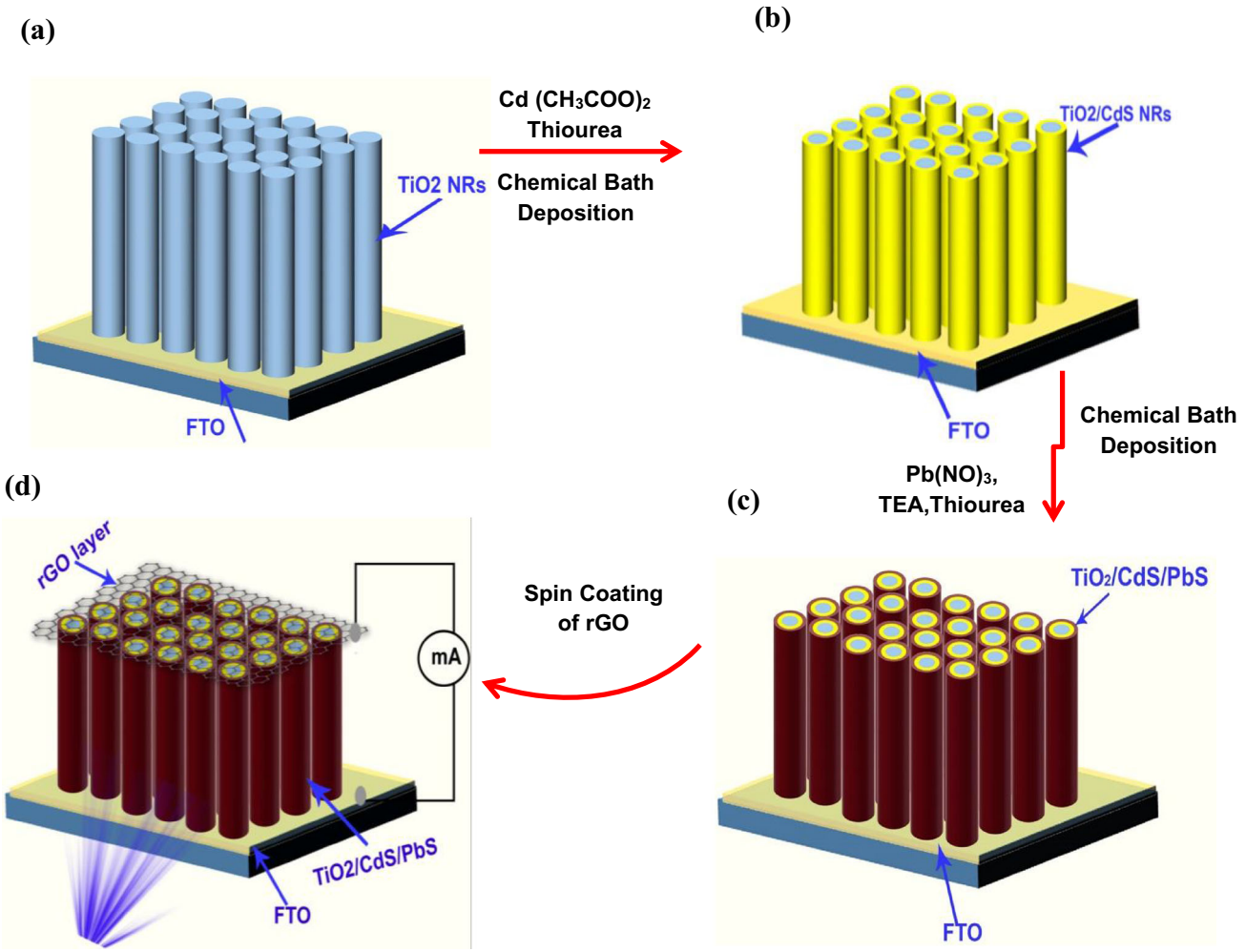

Figure 2. Schematic representation of fabrication of (**a**) TiO_2 NRs, (**b**) CdS-decorated TiO_2 NRs, (**c**) CdS/PbS-decorated TiO_2 NRs and (**d**) FTO/TiO_2 NRs/CdS/PbS/rGO final device structure.

at ~10 throughout the growth process. After PbS layer growth, all samples were thoroughly washed with DI and dried in air.

In this present study, photodetector properties of TiO_2/CdS/PbS NRs were analysed using FTO as a bottom electrode and rGO as the top conducting electrode. Graphene oxide (GO) flakes were grown by using well-known modified Hummer's method, and the detail growth process has been reported elsewhere [24–26]. Conductive-reduced GO flakes were prepared by a low-cost chemical method using ascorbic acid as a reducing agent [27]. To adjust the pH of the exfoliated GO solution (pH ~ 6), NaOH pellets (98%, Sigma Aldrich) were added followed by ultrasonication for 1 h. Then, another solution prepared by adding 10 g L-ascorbic acid (99%, Sigma Aldrich) in 100 ml DI water was poured slowly to the previous GO solution. The reduction process was conducted at 95°C for 1 h. The resultant black precipitates were filtered and washed with 1 M HCl solution followed by DI water to achieve neutral pH. Finally, the filtrate was freeze-dried to obtain rGO powder for further applications. To investigate the electrical conductivity of as-prepared rGO powder, small pellets (area $A = 1$ cm^2 thickness $t = 0.535$ mm) were made by laboratory hot press without any heat treatment. The electrical conductivity of rGO was calculated to be 3.93 S m^{-1}. For deposition of top rGO electrodes, at first rGO powders were dissolved thoroughly in *N*, *N*-dimethyl formamide solution. Afterwards, this rGO solution was spin coated on TiO_2/CdS/PbS NRs and dried in air to evaporate the solvent. Illustrative representation of synthesis of GO and rGO are presented in figure 1a. The scanning electron micrographs (SEM) of as-grown GO and rGO powders are presented in figure 1b and c, respectively. The schematic representation of the growth of TiO_2 NRs, CdS-coated TiO_2 NRs and TiO_2 NRs/CdS/PbS are presented in figure 2a, b and c, respectively. The final device structure after deposition of rGO on the NRs is illustrated in figure 2d.

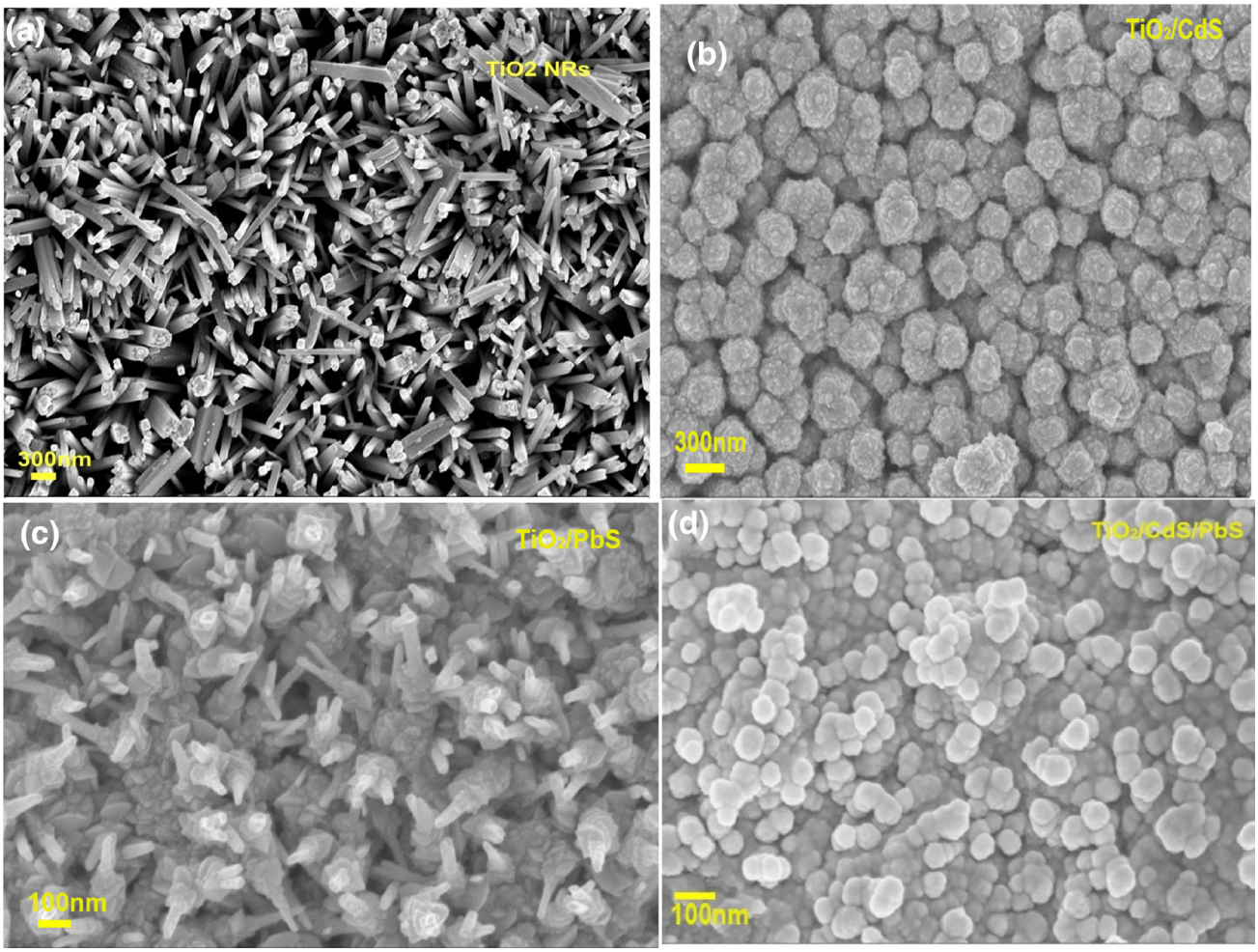

Figure 3. SEM micrograph of (**a**) pristine TiO_2 nanorods grown on FTO substrates, (**b**) TiO_2 nanorods after deposition of CdS by chemical bath deposition process, (**c**) TiO_2 nanorods after deposition of PbS by chemical bath deposition process, and (**d**) PbS/CdS-deposited TiO_2 NRs.

The surface morphology of TiO_2 NRs, CdS deposited on TiO_2 NRs, and PbS-deposited TiO_2 NRs and TiO_2 NRs/CdS/PbS were studied using Zeiss Sigma 300 scanning electron microscope (SEM). The crystalline nature and structural information of the samples were studied by using a Bruker D8 Advanced X-ray diffractometer. Optical absorption spectra of all samples were acquired by using a Shimadzu UV3600 plus UV-VIS-NIR spectrometer. Current–voltage (*I–V*) characteristics and photocurrents of all devices were studied using a dual channel Agilent, B2912A source measuring unit. Transient photoresponse results were obtained upon illumination of white light of intensity 100 mW cm^{-2} from solar a simulator (Enlitech, Taiwan). Spectral dependence of photocurrent of the samples were studied under incident of various wavelength of light (300–700 nm) from a monochromator attached with a white light source (Science Tech, Canada).

3. Results and discussion

Top view SEM micrographs of TiO_2 NRs, CdS-deposited TiO_2 NRs, PbS-deposited TiO_2 NRs and TiO_2 NRs/CdS/PbS are presented in figure 3a, b, c and d, respectively. Figure 3a represents the formation of vertically aligned TiO_2 NRs on FTO substrate with square top and average diameter is 80 nm. Figure 3b, c and d depict the SEM micrographs of TiO_2 NRs after deposition of CdS, PbS and CdS/PbS layers, respectively. The SEM images clearly show the deposition of CdS and PbS layers on NR surfaces. The presence of elements Cd, Pb, S at the surface of TiO_2 NRs were confirmed by EDX study during SEM imaging, and presented in supplementary figure S1a–c. The length of the TiO_2 NRs/CdS/PbS NRs has been estimated from cross-section SEM image, and presented in supplementary figure S2. The typical length of the NRs was found to be 1.23 μm. XRD spectra of pristine TiO_2 NRs, CdS-deposited

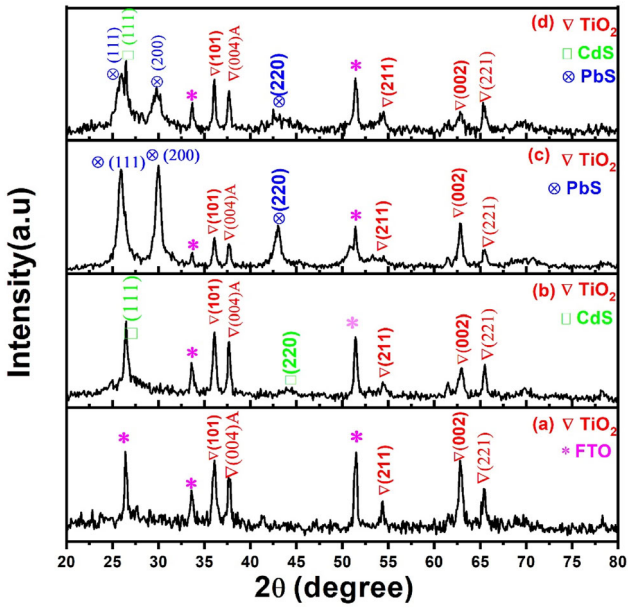

Figure 4. X-ray diffraction patterns of (**a**) pristine TiO_2 nanorods, (**b**) CdS-deposited TiO_2 NRs, (**c**) PbS-deposited TiO_2 NRs and (**d**) CdS/PbS-deposited TiO_2 NRs on FTO substrate.

TiO_2 NRs, PbS-deposited TiO_2 NRs and PbS/CdS-deposited TiO_2 NRs are shown in figure 4a, b, c and d, respectively. In figure 4a, the diffraction peaks at (101), (211), (002) and (221) planes represent the rutile phase (JCPDS#77-0440) [28] and the peak at (004) depicts the anatase phase of TiO_2 NRs (JCPDS#84-1285) [29]. It can be observed that, after CdS deposition the two peaks appeared at (111) and (220) planes (figure 4b), which confirmed the formation of cubic phase of CdS on TiO_2 NRs (JCPDS#75-1546) [30]. In figure 4c, all XRD peaks correspond to the crystal planes (111), (200), (220), which confirmed the growth of cubic structure of PbS on TiO_2 NRs (JCPDS#78-1899) [31]. The presence of both CdS and PbS peaks were also observed in TiO_2 NRs/CdS/PbS sample (figure 4d).

UV visible absorption spectra of TiO_2 NRs, CdS-deposited TiO_2 NRs, PbS-deposited TiO_2 NRs and TiO_2 NRs/CdS/PbS are plotted in figure 5a. TiO_2 NR shows strong UV absorption with absorption edge at 400 nm. On the other hand, the absorption edges of CdS-deposited TiO_2 NRs and PbS-deposited TiO_2 NRs are red shifted to visible region compared to pristine TiO_2 NRs. Interestingly, TiO_2 NRs/CdS/PbS showed enhanced absorption in wide spectral range, which is useful for broadband photodetector application [32,33]. The optical bandgaps (E_g) of the samples were calculated by using well-known Tauc's equation as shown below [34].

$$(\alpha h\nu)^{\frac{1}{n}} = C\left(h\nu - E_g\right), \tag{1}$$

where E_g is the energy bandgap of the samples, C is a constant, α the absorption coefficient and $h\nu$ the incident photon energy. The value of exponent n denotes the nature of transition. For direct allowed transition $n = \frac{1}{2}$ and for indirect allowed transition $n = 2$. In case of direct bandgap semiconductors, the bandgaps were calculated by

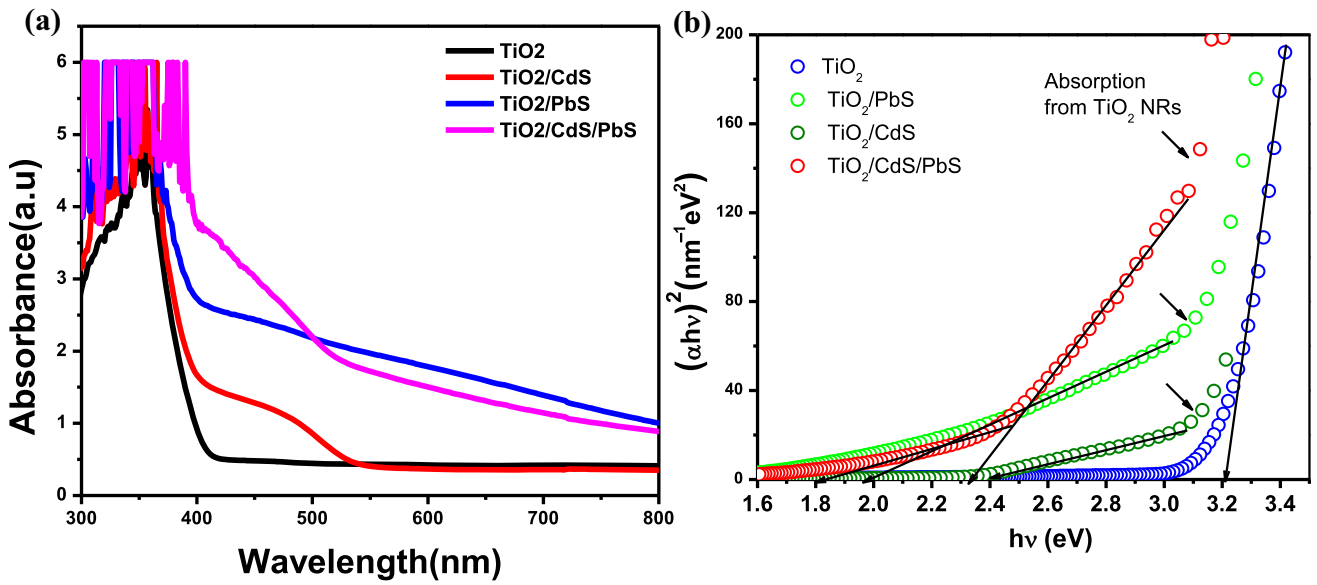

Figure 5. (**a**) UV–visible absorption spectrum of TiO_2 NRs, CdS-deposited TiO_2 NRs, PbS-deposited TiO_2 NRs and CdS/PbS-deposited TiO_2 NRs recorded in the wavelength range 300–800 nm. (**b**) Tauc's plots [$(\alpha h\nu)^2$ *vs.* $h\nu$] of TiO_2 NRs, CdS-deposited TiO_2 NRs, PbS-deposited TiO_2 NRs and PbS/CdS-deposited TiO_2 NRs.

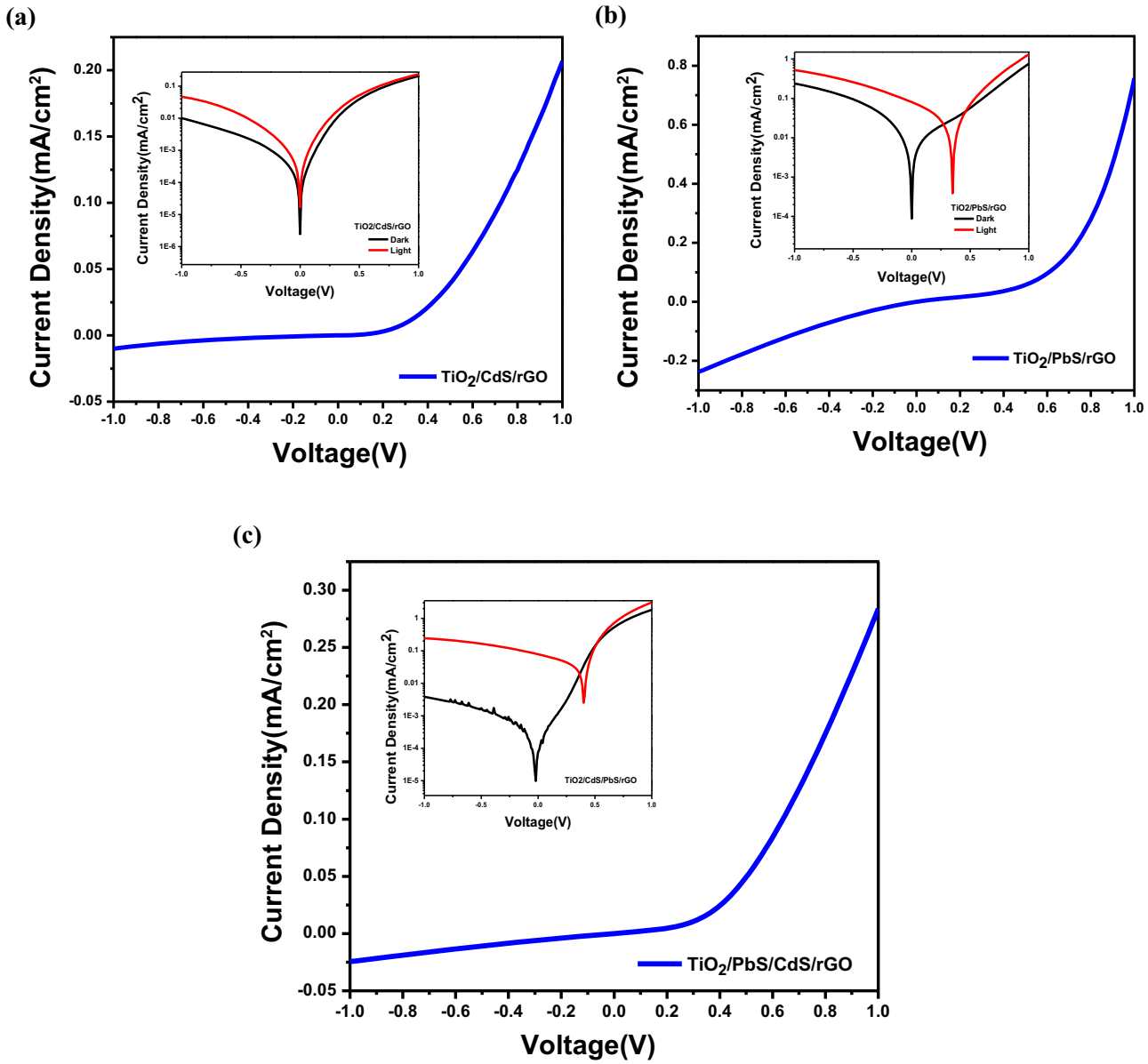

Figure 6. *J–V* characteristics of (**a**) TiO_2 NRs/CdS/rGO, (**b**) TiO_2 NRs/PbS/rGO and (**c**) TiO_2 NRs/CdS/PbS/rGO samples under dark condition. Semilogarithmic *J–V* characteristics of TiO_2 NRs/CdS/rGO, TiO_2 NRs/PbS/rGO and TiO_2 NRs/CdS/PbS/rGO samples under dark and broadband light source of intensity 100 mW cm^{-2} are presented in the insets.

extrapolating the linear region of the plots $(\alpha h\nu)^2$ *vs.* $(h\nu)$ to the energy $(h\nu)$ axis. Tauc's plots of all samples are presented in figure 5b. The calculated absorption edges of TiO_2 NRs, TiO_2 NRs/CdS, TiO_2 NRs/PbS were found to be 3.2, 2.4 and 1.9 eV, respectively. Interestingly, the Tauc's plot of TiO_2 NRs/CdS/PbS sample shows three distinct absorption edges. The absorption at 1.8 and 2.4 eV are accredited to the attachment of PbS and CdS on TiO_2 NRs surfaces, respectively. On the other hand, the absorption beyond 3.0 eV is ascribed to TiO_2 NRs.

To study the self-powered photodetection properties of TiO_2 NRs/CdS/PbS sample, the following three samples were fabricated. The samples are (i) FTO/TiO_2 NRs/CdS/rGO, (ii) FTO/TiO_2 NRs/PbS/rGO and (iii) FTO/TiO_2/CdS/PbS/rGO. The *J–V* characteristics of FTO/TiO_2 NRs/CdS/rGO, FTO/TiO_2 NRs/PbS/rGO and FTO/TiO_2/CdS/PbS/rGO devices under dark condition are shown in figure 6a, b and c, respectively. The semi-logarithmic *J–V* plots under dark and illumination of broadband light of intensity 100 mW cm^{-2} for the above samples are presented in the insets of figure 6. Both the control devices presented in figure 6a and b show rectifying nature with rectification ratio $\sim$20 and 3.4 at –1 V, respectively. On the other hand, FTO/TiO_2/CdS/PbS/rGO device (figure 6c) shows better rectification behaviour with rectification ratio $\sim$402 at –1 V bias, which is 20 times higher than FTO/TiO_2 NRs/CdS/rGO and 118

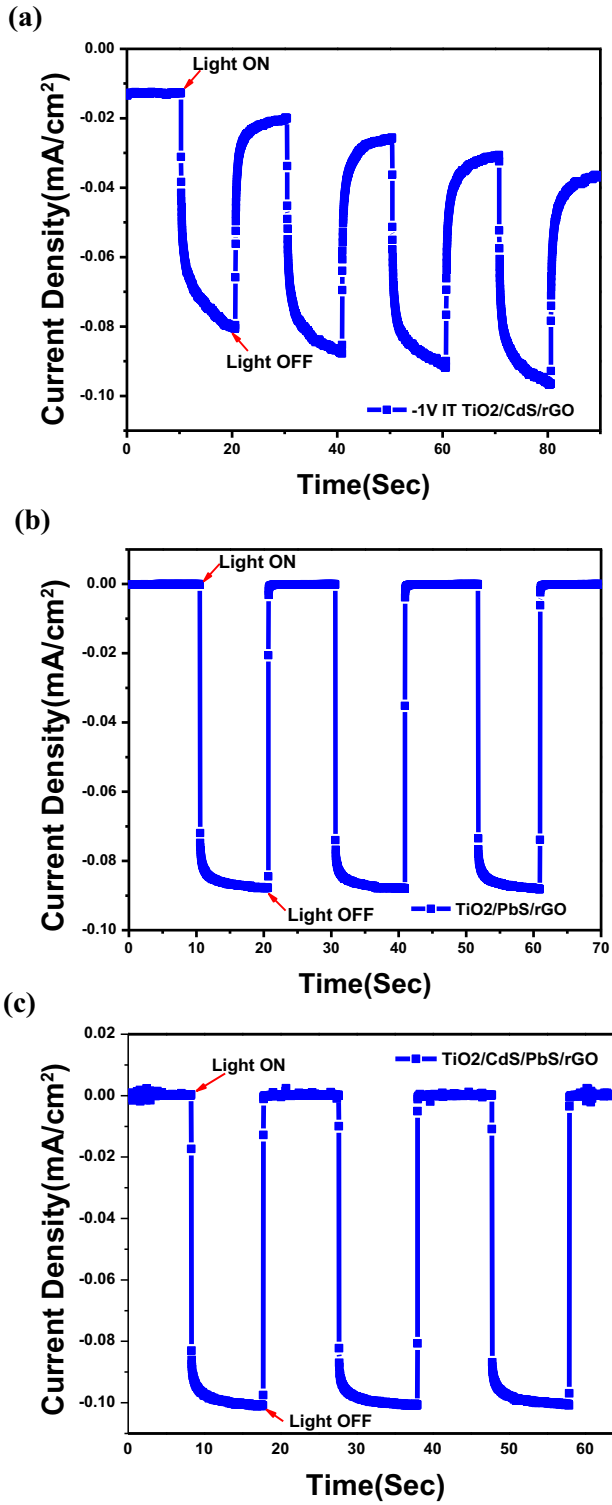

Figure 7. Transient photocurrent (*J*–*t* plot) of (**a**) TiO_2NRs/CdS/rGO sample at –0.1 V bias. (**b**) TiO_2NRs/PbS/rGO sample at 0 V bias. (**c**) TiO_2NRs/CdS/PbS/rGO sample at 0 V bias. Photocurrent response was measured under broadband light source of intensity 100 mW cm^{-2}.

times higher than FTO/TiO_2 NRs/PbS/rGO samples. After illumination of white light, the dark current increases for all

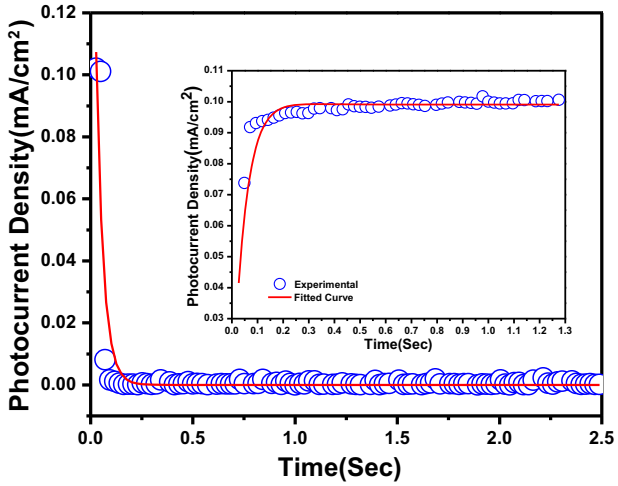

Figure 8. Experimental results (blue open circle) and fitted curves (solid red line) of response (inset) and recovery process of photocurrent of TiO_2 NRs/CdS/PbS/rGO sample.

devices. The change in dark current for TiO_2 NRs/CdS, TiO_2 NRs/PbS and TiO_2 NRs/CdS/PbS samples was observed to be 0.037, 0.28 and 0.31 mA cm^{-2}, respectively. More interestingly, TiO_2 NRs/PbS and TiO_2 NRs/CdS/PbS devices demonstrated self-powered photodetection. The power conversion efficiency (PCE) of all self-powered devices was estimated using the following equation [35]:

$$\eta = \frac{Voc \times J_{SC} \times FF}{P_{in}} \times 100\%, \quad (2)$$

where fill factor (FF) $= \frac{V_m \times J_m}{V_{OC} \times J_{SC}}$, V_{oc} is open circuit voltage, J_{SC} is short circuit current density, V_m and J_m are the maximum voltage and current density of *J*–*V* curve under illumination. P_{in} is the incident radiation of white light (100 mW cm^{-2}). The open circuit voltage (V_{oc}) and PCE of TiO_2 NRs/PbS/rGO sample were found to be ~0.35 V and 0.07%, respectively. On the other hand, the parameters V_{oc}, J_{SC} and PCE for TiO_2 NRs/CdS/PbS/rGO sample were observed to be ~0.40 V, 0.077 mA cm^{-2} and 0.16%, respectively. However, TiO_2 NRs/CdS sample did not show any self-powered photodetection property under illumination of light. The self-powered photodetection or photovoltaic property has been observed in TiO_2 NRs/PbS and TiO_2 NRs/CdS/PbS devices due to the formation of n–p junction at the interface of TiO_2/PbS and CdS/PbS, respectively. More importantly, the significant improvement of short circuit current (J_{SC}), open circuit voltage (V_{oc}) and PEC has been observed in TiO_2 NRs/CdS/PbS device due to broad photoabsorption and favourable band alignment at CdS/PbS junction [32,36,37].

The transient photoresponse of TiO_2 NRs/CdS, TiO_2 NRs/PbS and TiO_2 NRs/CdS/PbS samples are presented in figure 7a, b and c, respectively. The transient response of TiO_2 NRs/PbS and TiO_2 NRs/CdS/PbS devices were studied under ON/OFF of white light of intensity ~100 mW cm^{-2} at zero bias. However, in case of TiO_2 NRs/CdS

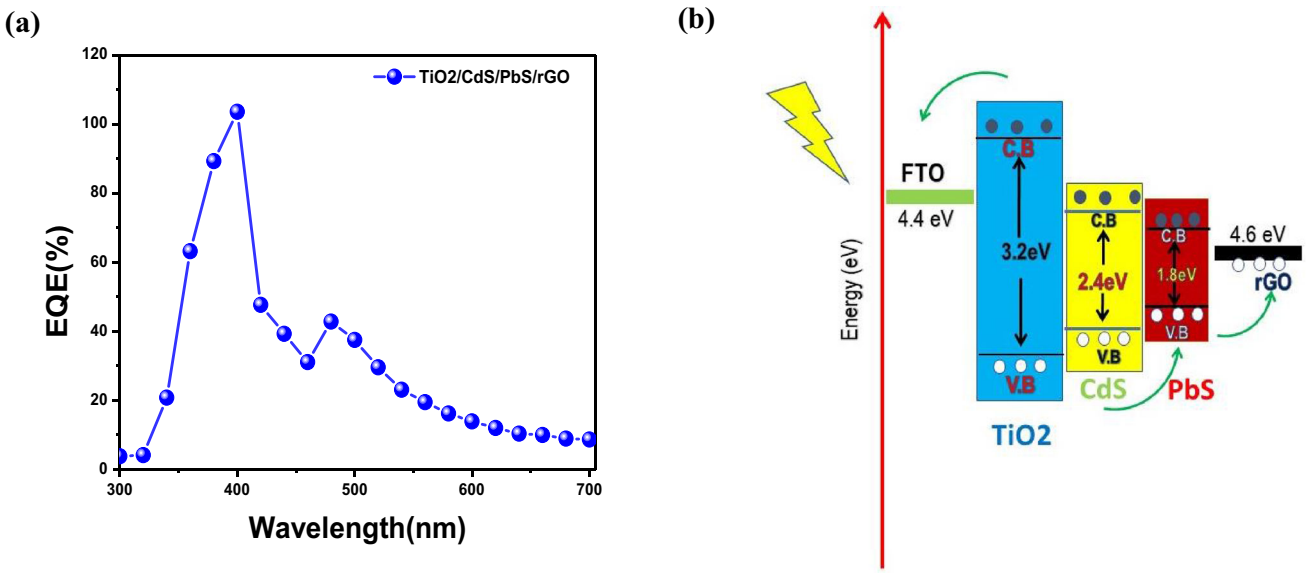

Figure 9. (**a**) EQE (%) *vs.* wavelength plot of TiO_2 NRs/CdS/PbS device at 0 V bias. (**b**) Schematic representation of carrier transport of FTO/TiO_2 NRs/CdS/PbS/rGO junction under white light illumination.

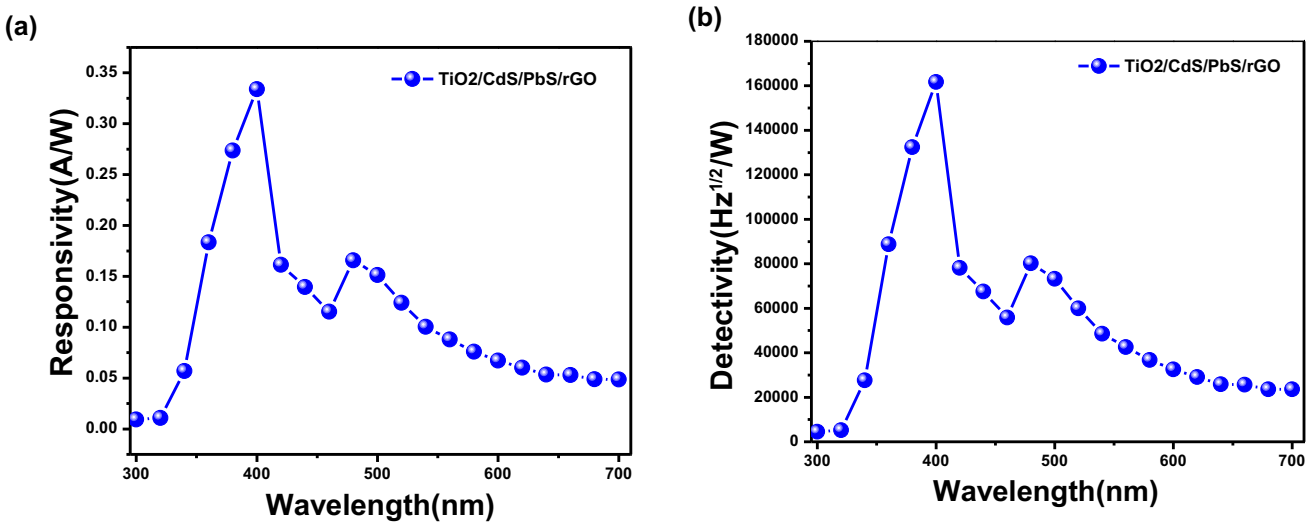

Figure 10. (**a**) Responsivity *vs.* wavelength plot of TiO_2 NRs/CdS/PbS/rGO device at 0 V. (**b**) Detectivity *vs.* wavelength plot of TiO_2 NRs/CdS/PbS/rGO under white light illumination.

sample, transient photocurrent response was measured at –1 V bias. It can be mentioned that, TiO_2 NRs/CdS sample did not show any self-powered photodetection and no photocurrent was detected at zero bias. From transient photoresponse, it is obvious that, the rise and fall of photocurrent of TiO_2 NRs/PbS junction is quite faster compared to TiO_2/CdS junction. More importantly, the ON/OFF ratio and rise/fall time significantly improves in case of TiO_2 NRs/CdS/PbS device. The ON/OFF ratio for TiO_2/PbS and TiO_2 NRs/CdS/PbS devices were found to be 2.21 and 30.17, respectively. The response and recovery time of TiO_2 NRs/CdS/PbS device was estimated from transient photoresponse results by using the following equations [7]:

$$J_R = \mathcal{A}(1 - e^{-t/\tau_1}) + \mathcal{B}(1 - e^{-t/\tau_2}), \quad (3)$$

$$J_D = \mathcal{A}e^{-t/\tau_1} + \mathcal{B}e^{-t/\tau_2}. \quad (4)$$

The symbols J_R and J_D are photocurrent densities at the time of rise and decay. $\mathcal{A}$ and $\mathcal{B}$ are constants, t is the ON/OFF time of light, τ_1 and τ_2 are time constants. The experimental data and fitted curve during rise and fall of photocurrent of TiO_2 NRs/CdS/PbS device are shown in figure 8. The calculated time constants during the rise of photocurrent are found to be $\tau_1 \sim 0.051$ s and $\tau_2 \sim 0.097$ s. Similarly, the photocurrent decay time constants are found to be $\tau_1 \sim 0.034$ s and $\tau_2 \sim 0.050$ s. The transient photoresponse of TiO_2 NRs/PbS device was also fitted with the

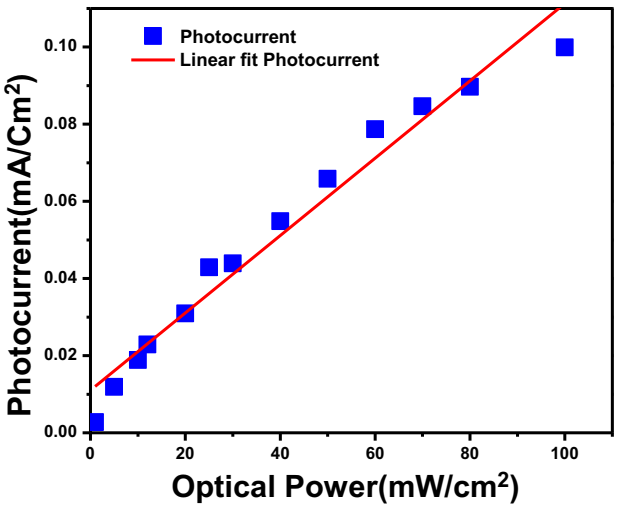

Figure 11. Photocurrent density *vs.* optical power density plot for TiO_2 NRs/CdS/PbS/rGO device. The optical power from a broadband light source was varied from 5 to 100 mW cm^{-2}.

above equations (supplementary figure S3). The extracted time constants during rise are $\tau_1 \sim 0.08$ s; $\tau_2 \sim 3.61$ s, while during decay are $\tau_1 \sim 0.22$ s and $\tau_2 \sim 25.38$ s, respectively. Obviously, TiO_2 NRs/CdS/PbS sample demonstrated fast rise and fall time compared to control samples.

To determine the ability to generate photocurrent under various wavelength of light, external quantum efficiency (EQE) measurement of TiO_2 NRs/CdS/PbS device was carried out at 0 V bias. EQE (%) has been estimated using the following equation [7].

$$\mathrm{EQE}(\%) = \frac{1240 J_\lambda}{\lambda P_\lambda} \times 100, \tag{5}$$

where J_λ is photocurrent density (mA cm^{-2}), λ the wavelength of monochromatic light (nm) and P_λ the monochromatic light intensity (mW cm^{-2}). Figure 9a shows the EQE (%) *vs.* λ plot of TiO_2 NRs/CdS/PbS device studied in the wavelength range 300–700 nm at 0 V bias condition. The EQE spectrum shows photocurrent response in UV-visible broad spectral range. Interestingly, two distinct peaks in EQE spectrum have been observed. The peak at 400 nm is attributed to UV photoabsorption for TiO_2, whereas the peak in visible region at 500 nm is ascribed to the photoabsorption from CdS and PbS layers [38,39]. The maximum EQE obtained was 105% at 400 nm. The EQE more than 100% may be accredited to multi-phonon generation in PbS layers [40].

The schematic band diagram and carrier transport mechanism is illustrated in figure 9b. The photovoltaic performance in TiO_2 NRs/CdS/PbS device is higher due to the favourable band alignment and cascade band formation [32]. When CdS layer was introduced in between TiO_2 and PbS, the energy gap of conduction band and valance band levels were reduced due to band cascade formation. Under illumination, electrons and holes are efficiently transported to the electrodes due to such stepwise structure. More importantly, strong visible photoabsorption of CdS enhances photocurrent of the TiO_2 NRs/CdS/PbS device. The responsivity (R_λ) and detectivity (D_λ) of the self-powered photosensing device were calculated using the following relations [41]:

$$R_\lambda = \frac{J_{\mathrm{light}} - J_{\mathrm{dark}}}{P_\lambda}, \tag{6}$$

$$D_\lambda = \frac{R_\lambda}{\sqrt{2qJ_{\mathrm{dark}}}}, \tag{7}$$

J_{light} and J_{dark} denote the current density at light and dark, respectively. P_λ is the incident light power density. Here, detectivity D_λ is measured in $Hz^{1/2}$ W^{-1} (or Jones) and q is the charge of electron. The responsivity (R_λ) and detectivity (D_λ) plots of TiO_2 NRs/CdS/PbS sample is shown in figure 10a and b, respectively. Similar to EQE spectrum, R_λ and D_λ also showed broad spectral response from 450 to 700 nm. The maximum responsivity and detectivity were observed at 400 nm and estimated to be 0.34 A W^{-1} and 162742.42 $Hz^{1/2}$ W^{-1}, respectively at 0 V bias.

To study the dependency of the device with intensity of light, photocurrents of the samples were measured under illumination of various intensity of white light (5–100 mW cm^{-2}) at zero bias. Figure 11 shows the change of photocurrent with optical power density. The photocurrent of the device varies in linear range with intensity of white light, which is attractive for broadband photosensing application. The photodetector properties of various TiO_2-based device are compared in table 1. From the table we

Table 1. Performance of various TiO_2-based self-powered photodetectors.

Device structure	Responsivity (A W^{-1})	External quantum efficiency (%)	Rise time (s)	Decay time (s)	Reference
SnO_2 nanoporous/TiO_2	0.113	42.6	0.007	0.006	[42]
TiO_2 NRs array	0.025	8.4	0.15	0.05	[23]
SnO_2/TIO_2NRs	0.145	49.2	0.037	0.015	[43]
TiO_2/MgO nanowire	0.23	—	0.01	0.01	[44]
TiO_2/CdS/PbS	0.34	105	0.09	0.034	This study

observe that our device TiO_2 NRs/CdS/PbS/rGO shows better responsivity at 0 V bias compared to the other results.

4. Conclusion

In summary, self-powered broadband photodetection was studied using PbS/CdS-decorated TiO_2 NRs grown on FTO-coated glass substrates. Growth, structural characterization and optical properties of PbS/CdS co-sensitized TiO_2 NRs have been studied in detail. Top electrode of the photodetector was made from rGO using ascorbic acid as reducing agent. TiO_2 NRs/CdS/PbS demonstrated broadband photosensing properties (350–700 nm) under zero bias. The major photodetector parameters such as EQE, R_λ and D_λ were studied without any external bias. The maximum responsivity (R_λ) and detectivity (D_λ) was obtained at 400 nm and estimated to be ~ 0.34 A W^{-1} and ~ 162742.42 $Hz^{1/2}$ W^{-1}, respectively. TiO_2 NRs /CdS/PbS/rGO device showed sharp rise and decay of photocurrent during ON/OFF of white light. The time constants during rise and decay of photocurrent were estimated to be $\tau_1 \sim 0.051$ s, $\tau_2 \sim 0.097$ s and $\tau_1 \sim 0.034$ s, $\tau_2 \sim 0.050$ s, respectively. The photodetector also demonstrated excellent self-powered nature with V_{oc} ~ 0.40 V, J_{SC} ~ 0.077 mA cm^{-2} and PCE $\sim 0.16\%$. This study indicated the potential use of CdS and PbS co-sensitized TiO_2 NRs for self-powered broadband photosensing applications.

Acknowledgements

We acknowledge the Central Research Facility (CRF) of NIT Agartala for XRD characterizations. We also acknowledge the DST-FIST project, Department of Physics, for UV-VIS-NIR spectroscopy measurements.

References

[1] Caratto V, Aliakbarian B, Casazza A A, Setti L, Bernini C, Perego P *et al* 2013 *Mater. Res. Bull.* **48** 2095
[2] Jagadale T C, Takale S P, Sonawane R S, Joshi H M, Patil S I, Kale B B *et al* 2008 *J. Phys. Chem. C* **112** 14595
[3] Bang J H and Kamat P V 2010 *Adv. Funct. Mater.* **20** 1970
[4] Jeng M-J, Wung Y-L, Chang L-B and Chow L 2013 *Int. J. Photoenergy* **2013** 1
[5] Gao Y, Xu J, Shi S, Dong H, Cheng Y, Wei C *et al* 2018 *ACS Appl. Mater. Interfaces* **10** 11269
[6] Wu S, Chen C, Wang J, Xiao J and Peng T 2018 *ACS Appl. Energy Mater.* **1** 1649
[7] Dhar S, Chakraborty P, Majumder T and Mondal S P 2018 *ACS Appl. Mater. Interfaces* **10** 41618
[8] Zheng W, Li X, He G, Yan X, Zhao R and Dong C 2014 *RSC Adv.* **4** 21340
[9] Lv P, Fu W, Mu Y, Sun H, Su S, Chen Y *et al* 2015 *J. Alloys Compd.* **621** 30
[10] Abbas M A, Basit M A, Park T J and Bang J H 2015 *Phys. Chem. Chem. Phys.* **17** 9752
[11] Yu L, Li Z, Liu Y, Cheng F and Sun S 2015 *J. Mater. Sci. Mater. Electron.* **26** 2286
[12] Guijarro N, Lana-Villarreal T, Lutz T, Haque S A and Gómez R 2012 *J. Phys. Chem. Lett.* **3** 3367
[13] Lee S, Flanagan J C, Kang J, Kim J, Shim M and Park B 2015 *Sci. Rep.* **5** 17472
[14] Pawar S B, Shaikh J S, Devan R S, Ma Y R, Haranath D, Bhosale P N *et al* 2011 *Appl. Surf. Sci.* **258** 1869
[15] Rekemeyer P H, Chang S, Chuang C-HM, Hwang G W, Bawendi M G and Gradečak S 2016 *Adv. Energy Mater.* **6** 1600848
[16] You D, Xu C, Zhang W, Zhao J, Qin F and Shi Z 2019 *Nano Energy* **62** 310
[17] Tian W, Wang Y, Chen L and Li L 2017 *Small* **13** 1701848
[18] Bai Z, Fu M and Zhang Y 2017 *J. Mater. Sci.* **52** 1308
[19] Hatch S M, Briscoe J and Dunn S 2013 *Adv. Mater.* **25** 867
[20] Peng L, Hu L and Fang X 2014 *Adv. Funct. Mater.* **24** 2591
[21] Wang Z L 2013 *ACS Nano* **7** 9533
[22] Wang Z L 2008 *Adv. Funct. Mater.* **18** 3553
[23] Xie Y, Wei L, Wei G, Li Q, Wang D, Chen Y *et al* 2013 *Nanoscale Res. Lett.* **8** 188
[24] Abdolhosseinzadeh S, Asgharzadeh H and Seop Kim H 2015 *Sci. Rep.* **5** 10160
[25] Wang Y, Chen Y, Lacey S D, Xu L, Xie H, Li T *et al* 2018 *Mater. Today* **21** 186
[26] Deka N, Chakraborty P, Chandra Patra D, Dhar S and Mondal S P 2020 *Mater. Sci. Semicond. Process.* **118** 105165
[27] De Silva K K H, Huang H-H and Yoshimura M 2018 *Appl. Surf. Sci.* **447** 338
[28] Wang Y, Li L, Huang X, Li Q and Li G 2015 *RSC Adv.* **5** 34302
[29] Sankapal B R, Salunkhe D B, Majumder S and Dubal D P 2016 *RSC Adv.* **6** 83175
[30] Yang X, Yang Y, Wang B, Wang T, Wang Y and Meng D 2019 *Solid State Sci.* **92** 31
[31] Mamiyev Z Q and Balayeva N O 2015 *Opt. Mater.* **46** 522
[32] Jiao J, Zhou Z-J, Zhou W-H and Wu S-X 2013 *Mater. Sci. Semicond. Process.* **16** 435
[33] Wang P, Zhang Z, Wang H, Zhang T, Cui H, Yang Y *et al* 2019 *J. Nanomater.* **2019** 1
[34] Viezbicke B D, Patel S, Davis B E and Birnie D P 2015 *Phys. Status Solidi B* **252** 1700
[35] Xu T and Yu L 2014 *Mater. Today* **17** 11
[36] Zhu Y, Wang R, Zhang W, Ge H and Li L 2014 *Appl. Surf. Sci.* **315** 149
[37] Li Y, Wei L, Chen X, Zhang R, Sui X, Chen Y *et al* 2013 *Nanoscale Res. Lett.* **8** 67
[38] da Silva Filho J M C, Ermakov V A and Marques F C 2018 *Sci. Rep.* **8** 1563
[39] Fu Y, Cao F, Wu F, Diao Z, Chen J, Shen S *et al* 2018 *Adv. Funct. Mater.* **28** 1706785
[40] Davis N J L K, Böhm M L, Tabachnyk M, Wisnivesky-Rocca-Rivarola F, Jellicoe T C, Ducati C *et al* 2015 *Nat. Commun.* **6** 8259

[41] Dhar S, Majumder T and Mondal S P 2017 *Mater. Res. Bull.* **95** 198

[42] Huang Y, Yu Q, Wang J, Li X, Yan Y, Gao S *et al* 2015 *Electron. Mater. Lett.* **11** 1059

[43] Chen D, Wei L, Meng L, Wang D, Chen Y, Tian Y *et al* 2018 *Nanoscale Res. Lett.* **13** 92

[44] Ni S, Yu Q, Huang Y, Wang J, Li L, Yu C *et al* 2016 *RSC Adv.* **6** 85951